

Measurement-Induced Landscape Transitions and Coding Barren Plateaus in Hybrid Variational Quantum Circuits

Gaurav Gyawali^{1,2†}, Sonny Rappaport^{1†}, Tiago Sereno^{3,4}, Michael J. Lawler^{3,1,2}

Laboratory of Atomic and Solid State Physics, Cornell University, Ithaca, NY, 14853, USA.

Department of Physics, Harvard University, Cambridge, MA 02138, USA.

Department of Physics, Applied Physics, and Astronomy, Binghamton University, Binghamton, NY 13902, USA.

School of Physics and Astronomy, University of Minnesota, Minneapolis, MN, 55455, USA.

Contributing authors: gg454@cornell.edu; str36@cornell.edu; tolivei3@binghamton.edu; mlawler@binghamton.edu;

[†]These authors contributed equally to this work.

Abstract

The entanglement-induced barren plateau is an exponential vanishing of the parameter gradients with system size that limits the practical application of variational quantum algorithms (VQA). A “landscape transition” from barren plateau to no-barren plateau was recently observed in monitored quantum circuits, hypothesized to coincide with the measurement-induced phase transition (MIPT) that separates the area-law states from the volume-law states. We argue from an information theory perspective that these are different transitions. This hypothesis is supported by a numerical study that includes cost-gradient variances, visualizations of the optimization runs and cost-landscape, and a quantum-classical channel mutual information measure. The results are evidence for a universal measurement-induced landscape transition (MILT) at $p_c^{\text{MILT}} \approx 0.2 < p_c^{\text{MIPT}}$ and that throughout $0 < p < p_c^{\text{MILT}}$, there is a finite quantum-classical channel mutual information in the limit of a large number of qubits. Unlike the barren plateau without measurements, a non-zero rate of measurements induces a coding barren plateau where, typically, information about the parameters is available to a local cost function despite a vanishing gradient.

Keywords: Quantum Optimization, Entanglement Phase Transition, Barren Plateau

1 Introduction

The age of noisy intermediate-scale quantum devices (NISQ) has seen the advent of quantum computers and simulators with nearly hundreds of qubits, noisy yet capable of serious computation¹. Although the long-term goal in quantum computing is to build error-corrected qubits, current noisy qubits still promise a potential quantum advantage. Variational quantum algorithms (VQA) have been central to much of the efforts in this direction²⁻⁴. VQA refers to the class of hybrid quantum-classical algorithms based on training parameterized quantum circuits by using a classical optimizer. They are desirable especially for the NISQ hardware because of their performance at low depth.

Practical implementation of the VQAs comes with its challenges—most prominently, the tradeoff between expressibility vs. trainability of the circuit. The success of a VQA depends on the expressibility of the variational ansatz under consideration, i.e., the ansatz must be able

to approximate the solution with reasonable accuracy⁵⁻⁷. Nevertheless, strong expressibility leads to poor trainability due to barren cost landscapes, a phenomenon dubbed barren plateaus (BP)⁷⁻¹¹. Characterized by the exponential vanishing of the gradient’s variance with the system size, BP typically arise in circuits deep enough to form a 2-design⁸. Thus, it poses a severe bottleneck in the scalability of the VQAs and their ability to solve complex problems.

Numerous strategies have been proposed to mitigate barren plateaus. These include problem-inspired¹² and adaptive ansatz¹³, local cost function⁹, pre-training¹⁴, identity-block initialization¹⁵, etc. Some recent studies have focused on the relationship between entanglement growth in random circuits and the onset of barren plateaus^{11,16,17}. Computing the many-body entanglement during the training process can be helpful to avoid BP via control of learning rate¹⁷. Nevertheless, the strategies proposed so far are either ad-hoc or increase the depth of the circuit, so we are still far from solving the BP problem.

Recently, it was observed that a “landscape” transition can occur if measurements are added to a VQA ansatz¹⁸. Without measurements, the entanglement entropy of a quantum chain undergoing local unitary evolution grows linearly in time until it thermalizes to a volume-law entangled state¹⁹. In contrast, local measurements tend to disentangle the system via wavefunction collapse. A dynamical competition between these two circuit components leads to a phase transition between phases with different system size scaling of entanglement in a variety of models, a topic of wide interest in recent years dubbed the measurement-induced phase transition (MIPT)^{20–27}. This phase transition suggests we can control entanglement and the BP with measurements and supports the observation of a landscape transition that appears to coincide with the MIPT¹⁸.

In this work, we argue the MIPT and the measurement-induced landscape transition (MILT) are different phase transitions on information theoretic grounds. We support this hypothesis with extensive numerical evidence on cost function gradient variances, landscape visualizations, and information-theoretic measures. We observe that the MILT appears seemingly at a universal critical measurement probability rate p_c^{MILT} across different ansatzes, at a lower rate than the MIPT and does not require post-selection to identify. Yet we find that projective measurements and post-selection can be exploited to assist optimization. Perhaps most strikingly, the mutual information reveals the $0 < p < p_c^{\text{MILT}}$ phase is a coding barren plateau, a phase where information about the parameters reaches the local cost function even though the gradient vanishes.

1.1 Information theory of optimization

There is an information-theoretic way to understand quantum optimization. In principle, the problem is straightforward. One parameterizes a space of wave functions $|\psi(\boldsymbol{\theta})\rangle$, with $\boldsymbol{\theta}$ a multidimensional array of real numbers. Then, by choosing initial values for $\boldsymbol{\theta}$, and quantum computing the gradient of the cost function $\langle \psi(\boldsymbol{\theta}) | \hat{O} | \psi(\boldsymbol{\theta}) \rangle$, one takes small steps down-hill in the cost landscape until reaching a local minimum. But we can turn this around, as in Fig. 1, and view it as a communication problem.

Suppose Alice is the person responsible for choosing the parameters. Alice chooses a parameter $\boldsymbol{\theta}$ from a classical distribution $p_A(\boldsymbol{\theta})$ and sends many copies of it to Bob via a classical-quantum channel $\mathcal{N} : \boldsymbol{\theta} \mapsto \hat{\rho}_\theta$ (see chapter 5 of Holevo²⁸ for a definition of classical-quantum channels). Bob has access to these quantum states via POVM measurements $\{\hat{E}_i\}$ associated with the eigenbases of the to-be-optimized observable \hat{O} with which he tries to decode the classical information sent by Alice. Fixing the measurements that Bob can perform to a single projective basis then reduces the classical-quantum channel to the classical channel

$$p(x | \boldsymbol{\theta}) = \text{Tr}[\hat{\rho}_\theta \hat{E}_i]. \quad (1)$$

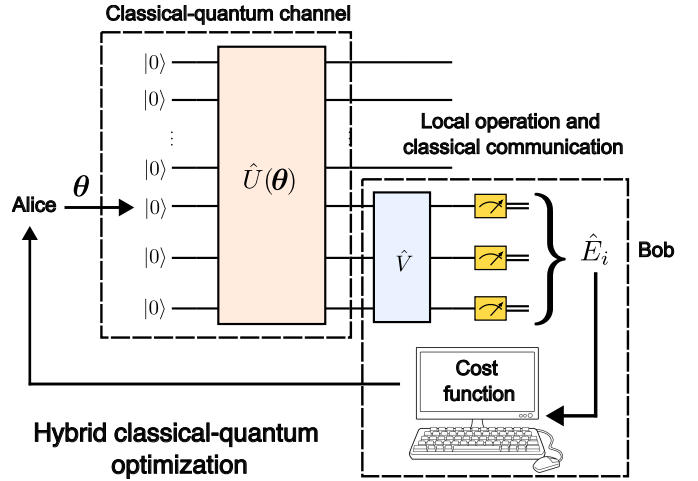


Fig. 1: An information theory perspective of optimization in two steps. Alice draws parameters from $p_A(\boldsymbol{\theta})$, and sends copies of them to Bob via a classical-quantum channel $\boldsymbol{\theta} \mapsto \hat{\rho}_\theta$. Bob then performs measurements $\{\hat{E}_i\}$ on $\hat{\rho}_\theta$, which he uses to compute the cost function, and sends the results back to Alice, which amounts to a local operation and classical communication (LOCC).

Finally, the measurement outcomes are used to compute the cost function, a computation whose results are sent back to Alice via a (noiseless) classical communication channel. The steps between Bob’s local measurements and sending the results back to Alice constitute a local operation and classical communication (LOCC).

If any intermediate measurements occur in the circuit, we consider both cases where the measurement outcomes may or may not be available to Bob. If the measurements are available to Bob, then the classical-quantum channel becomes $\boldsymbol{\theta} \mapsto \hat{\rho}_{\boldsymbol{\theta}, \mathcal{M}}$ where $\hat{\rho}_{\boldsymbol{\theta}, \mathcal{M}}$ is the quantum state formed from the collapse of the wave function. Otherwise, the channel remains the same as above, but the state ρ_θ has thermalized.

This information theory perspective allows us to illustrate the measurement-induced landscape transition. If no measurements take place, the classical-quantum channel $\boldsymbol{\theta} \mapsto \rho_\theta$ encodes Alice’s classical information into a highly entangled state, making it difficult for Bob to decode from Bob’s local measurements $\{\hat{E}_i\}$. This difficulty is the cause of the BP⁸. Based on this intuition, BP should be accompanied by an exponential reduction of the channel’s capacity to transmit information between Alice and Bob. If many intermediate measurements are performed, and these measurement outcomes are known to Bob, then a quantum zeno effect takes place²⁰. The many measurements render the state $\hat{\rho}_{\boldsymbol{\theta}, m}$ largely independent of earlier parameters $\boldsymbol{\theta}$ but the state no longer has a high degree of entanglement. If the measurement outcomes are unknown to Bob, then the thermalization of $\hat{\rho}_\theta$ takes place and introduces significant noise. These phenomena have different system size scaling, so we expect a phase transition between them. Thus, one can hope for an optimal trade-off between no measurements and many

measurements, perhaps at a critical point between the two, where optimization is substantially improved.

We can contrast this information-theoretic view of optimization with that of the MIPT^{26,27}. In a MIPT, Alice chooses a quantum state ρ and sends this to Bob via a quantum channel $\hat{\rho} \mapsto \hat{\rho}'$. Bob then needs to *decode the quantum information* sent by Alice with knowledge of any measurement outcomes that took place in the channel, and Bob typically measures the entanglement of the state to identify the phase transition, a resource not available in optimization. An MIPT is therefore different on information theoretic grounds from that of MILT.

1.2 Optimization problems and post-selection

The goal of finding the desired ground state in the space of an exponentially large Hilbert space is an arduous task. An ideal variational ansatz capable of achieving it must be able to create a complex network of entanglement between the qubits, yet explore only a polynomial-sized space near the solution point. But such expressibility often comes at the price of more variational parameters and a landscape plagued with BPs and narrow gorges⁹.

We need to choose several ansatzes to capture the typical behavior of landscape transitions and their information-theoretic properties. Since the building blocks of any variational ansatz are single qubit rotations and entangling gates, we can choose these gates and the connectivity between the qubits to match the device architecture and obtain a hardware-efficient ansatz (HEA)²⁹. Although flexible and highly expressible, optimizing them for a specific problem can be challenging in practice. Thus, it is often useful to turn to problem-inspired ansatzes, for example, quantum approximate optimization algorithm (QAOA)³⁰ for combinatorial optimization problems and Hamiltonian variational ansatz (HVA)^{31,32} for finding the ground state. For problems involving long length scales, renormalization group-like flows can be implemented with the quantum convolutional neural network (QCNN)³³, found to be free from BP³⁴. For certain problems, one may also choose how the various building blocks in the circuits are stacked. An example of this paradigm is the ADAPT-VQE algorithm^{35,36}, which is also BP-free¹³. Our work is inspired by the quest to improve existing ansatzes by introducing measurement gates that allow control over entanglement growth in the circuit.

We focus specifically on the following three ansatzes:

- (a) Hardware efficient ansatz 1 (HEA1)
- (b) Hardware efficient ansatz 2 (HEA2)
- (c) XXZ Hamiltonian variational ansatz (XXZ-HVA)

The ansatzes chosen are similar to those used in the paper by Wiersema *et al.*¹⁸, in part to provide a direct comparison of our results. Specifically, our HEA2 and XXZ-HVA ansatz is nearly identical to their HEA and XXZ-HVA. All ansatzes consist of several layers, in which unitary gates are applied, possibly followed by projective measurements with probability p on each qubit, a setup commonly used in the measurement-induced phase transition literature. These ansatzes are all shown in Fig. 2.

2 Results and Discussion

We now turn to our numerical results. In what follows, we provide evidence the MILT and MIPT are different phase transitions, and there exists a coding barren plateau phase in the range $0 < p < p_c^{\text{MILT}}$. We will do so by observing the variances in cost function gradients, visualizations of the optimization process, and information-theoretic measures of the optimization process.

2.1 Landscape transitions observed in mixed and projective gradients

We have computed variances of cost function gradients, a key indicator of BPs⁸, systems sizes up to 18 qubits, and circuit depths up to 100 layers of each ansatz presented in Fig. 2. Before presenting the results, we carefully define the cost functions we use.

The intermediate measurements in hybrid variational quantum circuits yield different outcomes for each run. We can compute the expectation value of observables either by (i) post-selecting for a specific outcome set \mathbf{M} or (ii) averaging over all the measurement outcomes. Post-selection requires exponentially many samples in the number of measurement gates. However, if the expectation value is averaged over all the measurement outcomes, it corresponds to computing the expectation value with respect to the average density matrix. Thus, we define two types of cost functions, *projective* cost functions computed with post-selected measurement outcomes, and *mixed* cost functions computed ignoring measurement outcomes.

The *projective cost function* refers to the expectation value of an observable \hat{O} calculated for a post-selected wave function. Consider, for example, a circuit consisting of a layer of unitary $\hat{U}(\boldsymbol{\theta})$ and a projective measurement. A variational circuit will have many such unitary and measurement layers, but the same results can be used for the deeper circuit as we will show in SI 3.3. We define the projective cost function, post-selected for outcome \mathbf{M} as follows:

$$C_{\mathbf{M}}(\boldsymbol{\theta}) = \langle \psi_{\mathbf{M}}(\boldsymbol{\theta}) | \hat{O} | \psi_{\mathbf{M}}(\boldsymbol{\theta}) \rangle = \text{Tr} \left[\hat{O} \hat{\rho}_{\mathbf{M}} \right], \quad (2)$$

where $\rho_{\mathbf{M}}(\boldsymbol{\theta}) = |\psi_{\mathbf{M}}(\boldsymbol{\theta})\rangle \langle \psi_{\mathbf{M}}(\boldsymbol{\theta})|$ is the state projected onto measurement outcome \mathbf{M} with projection operator $\hat{P}_{\mathbf{M}}$, and probability $p_{\mathbf{M}}$ as given below:

$$|\psi_{\mathbf{M}}(\boldsymbol{\theta})\rangle = \frac{|\tilde{\psi}_{\mathbf{M}}(\boldsymbol{\theta})\rangle}{\sqrt{p_{\mathbf{M}}(\boldsymbol{\theta})}} = \frac{\hat{P}_{\mathbf{M}} \hat{U}(\boldsymbol{\theta}) |0\rangle}{\sqrt{\langle 0 | \hat{U}^\dagger(\boldsymbol{\theta}) \hat{P}_{\mathbf{M}} \hat{U}(\boldsymbol{\theta}) |0\rangle}}. \quad (3)$$

Likewise, the *mixed cost function* is obtained by averaging the expectation value of an observable \hat{O} over all possible measurement outcomes i.e.,

$$C(\boldsymbol{\theta}) = \mathbb{E}[C_{\mathbf{M}}(\boldsymbol{\theta})] = \sum_{\mathbf{M}} p_{\mathbf{M}}(\boldsymbol{\theta}) \langle \psi_{\mathbf{M}}(\boldsymbol{\theta}) | \hat{O} | \psi_{\mathbf{M}}(\boldsymbol{\theta}) \rangle \quad (4)$$

$$= \text{Tr} \left[\hat{O} \hat{\rho}(\boldsymbol{\theta}) \right]. \quad (5)$$

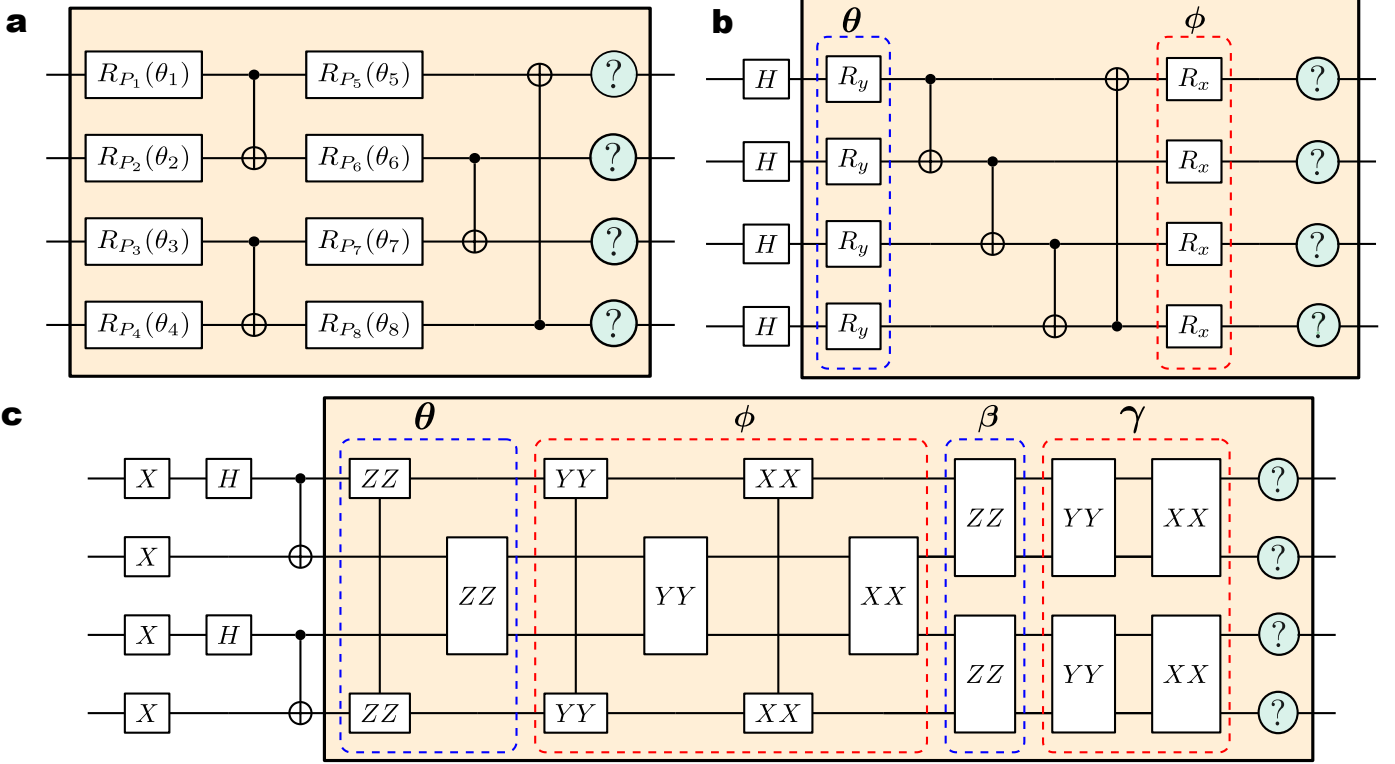


Fig. 2: A single layer of the ansatzes examined in this paper. The light-orange shaded regions in each diagram are those repeated in every layer, whereas those outside are used only for the initial layer. Measurement gates, represented by the light-green circles, are randomly placed with probability p after each layer except the last. **a** HEA1: Apply a R_{P_i} gate to each qubit, followed by CNOT pairs on even paired qubits, followed by applying more R_{P_i} gates to each qubit, followed by applying CNOT pairs to odd paired qubits. Each R_{P_i} gate represents a random rotation gate generated by a Pauli operator P_i , parameterized by an angle θ_i . **b** HEA2 and **c** XXZ-HVA are heavily inspired by the ansatzes used in Wiersema *et al.*¹⁸. Note that the parameters are applied uniformly across all the qubits in **b** and **c**. Although shown for only four qubits, each ansatz can be generalized to any even number of qubits.

In other words, mixed cost function is the expectation value with respect to the measurement-averaged density matrix $\hat{\rho} = \sum_{\mathbf{M}} p_{\mathbf{M}} \hat{\rho}_{\mathbf{M}}$.

The post-selected (projective) wavefunctions are free from barren plateaus at some carefully chosen probability range of placing a measurement gate. Fig. 3 clearly shows barren plateaus at $p = 0$. Nevertheless, as we increase the probability of measuring, the barren plateau seems to get less severe, i.e., the gradient goes from exponential scaling with system sizes to some constant over a probability range (somewhere around $p = 0.2$), then decays exponentially with probability until it hits the machine’s precision. This exponential decay differs from barren plateaus because the exponential decay of gradients with the system size characterizes barren plateaus. Note that projective gradients in Fig 3 are averaged over various measurement outcomes, so the error bars are higher for more measurement gates as the number of possible outcomes scales like 2^M , where M is the number of measurement gates. We refer to this region of exponentially small gradients as the “quantum Zeno” phase, a term coined by Li *et al.*²⁰ for quantum states that are frequently measured, and hence stalled close to an eigenstate of the measurement operator. Moreover, we are post-selecting for outcomes \mathbf{M} ; consider $\mathbf{M} = \{0, 0 \dots, 0\}$ and $p = 1.0$, then the expectation value of an operator \hat{O} is always

going to be $\langle 00 \dots 00 | \hat{O} | 00 \dots 00 \rangle$ with no dependence on the variational parameters. The measurements essentially cut the communication between the parameters at the beginning of the circuit and the end, hence diminishing gradients.

The value of probability at which the barren plateau disappears depends on two factors: (i) the depth of the circuit and (ii) ansatz. The effect of depth on the projective gradients is to shift the turning point towards $p = 0$, eventually stopping at $p \approx 0.2$. The dependence on the ansatz is much weaker than the dependence on the circuit depth. As a result, we don’t find the landscape transition coinciding with the measurement-induced phase transition in our projective gradients as reported by Wiersema *et al.*¹⁸. To understand this observation, we note that the gradient with respect to a parameter θ is a linear observable:

$$\partial_{\theta} \langle \hat{U}_1^{\dagger}(\theta) \hat{U}_2^{\dagger} H \hat{U}_2 \hat{U}_1(\theta_1) \rangle = i \langle 0 | \hat{U}_1^{\dagger} [\hat{P}, \hat{U}_2^{\dagger} \hat{H} \hat{U}_2] \hat{U}_1 | 0 \rangle, \quad (6)$$

where we have taken $\hat{U}_1 = e^{-i\theta \hat{P}}$, and U_2 is an arbitrary that follows U_1 . The variance of the linear observable is a classical average of this linear observable squared. MIPT can neither be observed in linear observables nor their classical averages. Therefore, a new phase diagram different from MIPT is required to depict the trainability

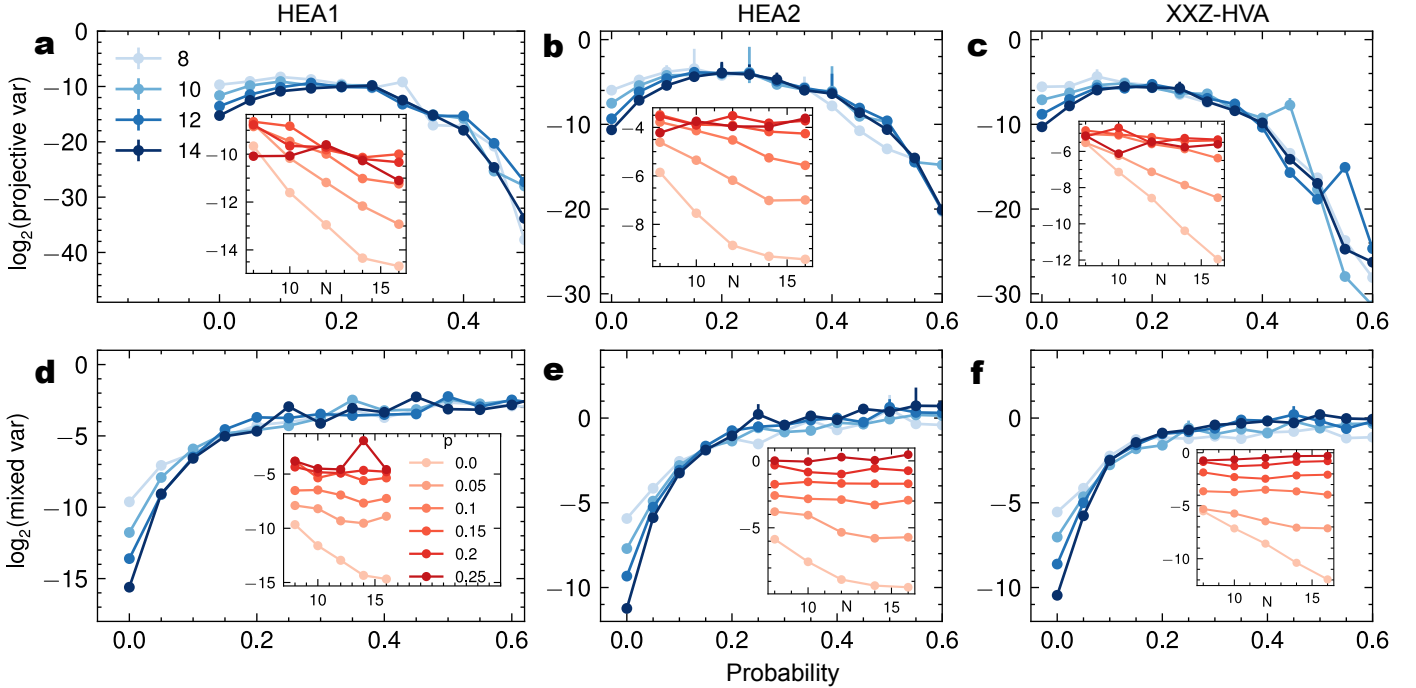


Fig. 3: Log of the variance for projective and mixed gradients. Top panels (a, b, c) show the projective gradient’s variance vs. measurement probability for HEA1, HEA2, and XXZ-HVA ansatzes respectively for system sizes $N = 8 - 16$ at constant depth 16. Inset shows the projective variance as a function of the number of qubits (N), showing that the barren plateau becomes less severe with higher measurement probability for $p \approx 0 - 0.2$. Nevertheless, the projective gradient decays exponentially with probability after a certain value. Similarly, the bottom panels (d, e, f) show the mixed gradient’s variance for HEA1, HEA2, and XXZ-HVA ansatzes, respectively. Insets show the variance as a function of the number of qubits, showing the barren plateau becomes less severe with more measurement gates and completely disappears around $p = 0.15$ for all ansatzes.

of the monitored variational quantum circuits. Based on the numerical evidence, we construct this phase diagram in Fig. 7 that we will discuss in Sec. 2.4

The mixed gradients always seem to have the same basic structure i.e., the gradient grows with the probability of measurement and plateaus to a constant value after around $p = 0.2$. Exponential vanishing of gradients i.e, BP in this case is compensated for by summing over exponentially many measurements. Unlike the projective gradient, the location of the turning point is independent of the depth of the ansatz. Here, we still destroy the barren plateau at the same critical value as in the case of projective gradients but this doesn’t seem useful for optimization.

2.2 Landscape visualization of the optimization process

In the previous section, we focused on the optimization problem at the beginning of the optimization algorithm. We did so by examining the variance of the gradients of different cost functions computed on randomly generated initial states. This analysis can explain the difficulty of optimizing a circuit at the beginning of the optimization loop, but it does not directly address what happens at later optimization stages. Here we present optimization traces that show the path the algorithm takes through the cost landscape and seek to determine if measurements significantly alter these paths and whether a landscape

transition is good for optimization in practice. We end with a visualization of the cost landscape near a local minimum using a technique common in machine learning literature for visualizing loss landscapes of neural networks³⁷.

In short, we find that the optimization traces benefit from the improved variance of hybrid variational ansatzes, thus mitigating the BP problem. The optimization runs were carried out for the projective cost function corresponding to the HEA2 ansatz for $\hat{Z}_0\hat{Z}_1$ and XXZ Hamiltonians. For the $\hat{Z}_0\hat{Z}_1$ Hamiltonian, the cost function depends only on the first two qubits, and the initial computational basis state satisfies the minimum value. Nevertheless, optimizing a circuit with a depth of 20 to get this simple product state is challenging because of the BP, as shown in Fig. 4. Inserting measurement gates results in the optimization traces exploring various energies, with some reaching the minima. For higher probabilities, the optimization traces again get stuck at some parameter values. However, most happen to satisfy the minimum value because of the simple nature of the cost function with enormously degenerate global minima.

In SI 2, we present optimization traces on the XXZ Hamiltonian ground state problem, which show similar but more complex behavior. In general we find measurements seem to help for some ansatzes more than others. For the HEA2 ansatz, they seem to work well, but for HEA2 with flexible parameters (not shown), and the XXZ the results are more mixed.

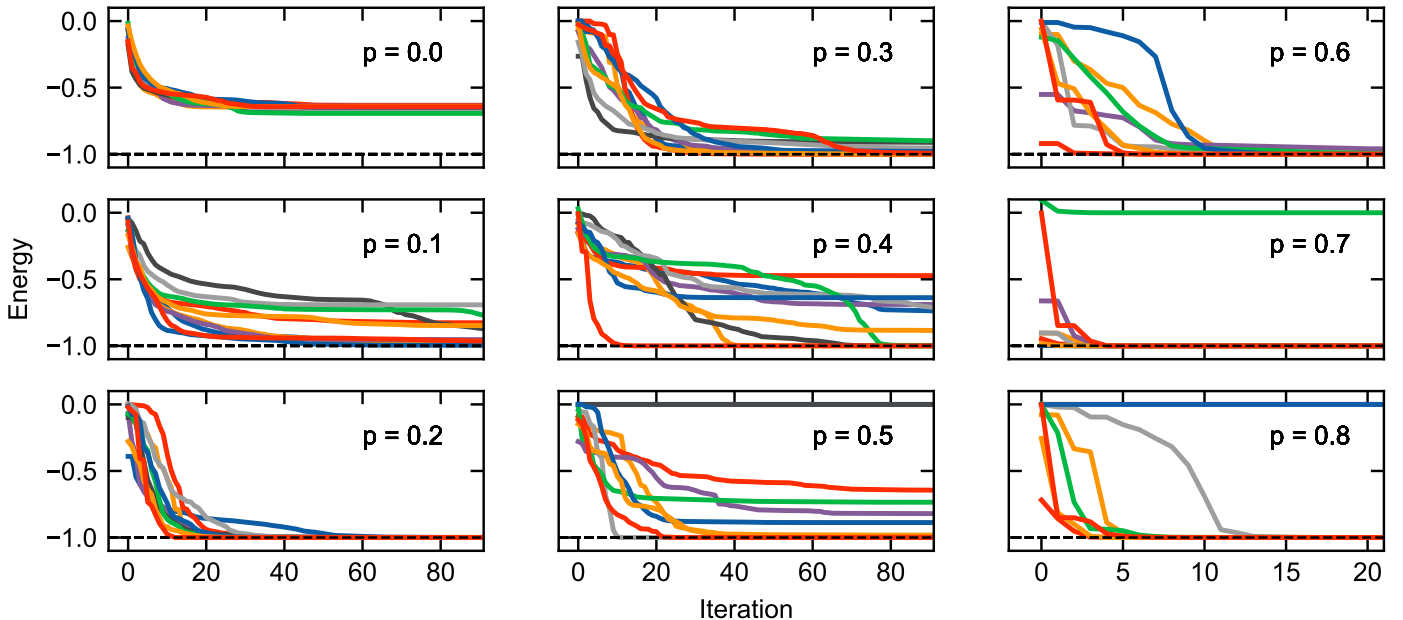


Fig. 4: Optimization with measurement and post-selection. Optimization traces shown for a 8-qubit system with cost function $\hat{Z}_0\hat{Z}_1$. Each sub-figure corresponding to a measurement probability between 0 and 0.8 contains traces from 10 individual optimization runs carried out for the HEA2 ansatz with depth 20. The dashed line shows the exact ground state energy.

Although the variance of the mixed gradient increases with an increase in the number of measurement gates, they optimize poorly. The optimization trace (not shown here) gets noisier with the probability of placing a measurement. This suggests a noisy cost landscape for the mixed cost function.

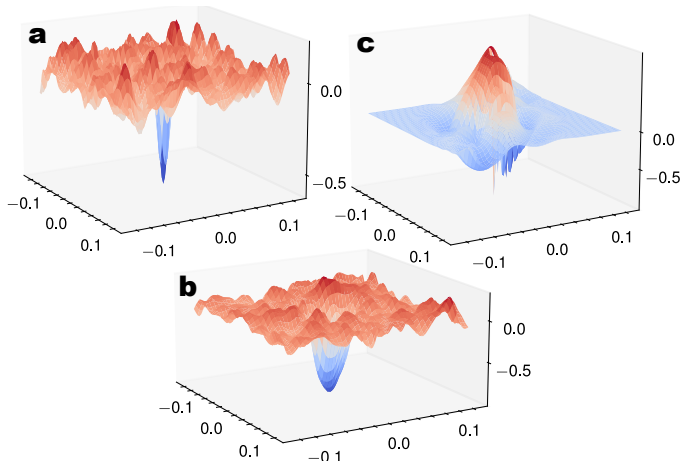


Fig. 5: Cost landscape visualizations of the monitored HEA2 hybrid variational circuits with $\hat{O} = \hat{Z}_0\hat{Z}_1$. Visualizations are produced by optimizing the circuit and then plotting $C(\theta)$ along two random directions in θ -space, where the origin is the minima achieved. **a** no measurements showing a large barren plateau with a narrow path to the optimal state, **b** measurement probability $p = 0.1$ showing a small barren plateau with a broad path to the optimal state, and **c** $p = 0.8$ showing the quantum Zeno region, where the landscape is smooth and flat with broad suboptimal minima and a large volcano-like entrance to the optimal state.

Since the optimization traces are complex, we turned to visualizing the cost landscape near a local minimum. Following Ref.³⁷, we can visualize the cost landscape by randomly choosing two directions in Alice’s parameter space and plotting the cost function on the plane spanned by these essentially orthogonal directions. The results for the HEA2 cost function are presented in Fig. 5. In the absence of measurements, they show a rough BP with a very sharp drop to the local minima. This sharp drop broadens in the presence of measurements while the BP nevertheless persists. Then at a large measurement rate, in the quantum Zeno phase, the BP is absent, the landscape is smooth, and a volcano-like entrance guards the path to the minimum, explaining the difficulty of finding this minimum and getting out of it once one is inside.

2.3 Entanglement vs Landscape phase transitions

In section 1.1, we argued that the MILT is different from the MIPT since the two involve different types of communication channels. We begin with a careful analysis of the MIPT in the three ansatzes we have been examining in this manuscript. These results show that in our example systems $p_c^{\text{MILT}} < p_c^{\text{MIPT}}$ and so the two transitions do not coincide. We then provide evidence that the MILT is a phase transition in an information-theoretic property of optimization problems and that the measurement-induced barren plateau phase is a coding phase suggesting a solution to the barren plateau exists if a decoder can be constructed to extract the dependence of the cost function on the parameters.

We begin with identifying the MIPT in our three ansatzes. To do so, we rely on computing the subsystem

Ansatz	p_c^{MIPT}	ν
HEA1	0.42 ± 0.02	1.18 ± 0.03
HEA2	0.48 ± 0.01	1.25 ± 0.04
XXZ-HVA	0.27 ± 0.02	1.26 ± 0.06

Table 1: Critical measurement rate p_c^{MIPT} and correlation length exponent ν The results were obtained numerically by finite size scaling of the von-Neumann entropy shown in SI.

von-Neumann entropy to identify the entanglement phase transition. We note that two of them have been studied previously by Wiersema et. al¹⁸. It is crucial that the entropy is calculated for the post-selected states and averaged over various circuit realizations and measurement outcomes rather than vice-versa. For a specific circuit realization, the von Neumann entropy of a subsystem A is given by

$$S(A) = \text{Tr}[\hat{\rho}_A \log_2 \hat{\rho}_A], \quad (7)$$

where $\hat{\rho}_A = \text{Tr}_{\bar{A}}[|\psi\rangle\langle\psi|]$.

When the measurement gates are placed with high probability ($p > p_c^{\text{MIPT}}$), the resulting state lies close to a trivial product state in the Hilbert space, and the late-time entanglement exhibits area-law scaling with the subsystem size i.e. $S(A) \propto |\partial A|$. However, if the measurement gates are too sparse ($p < p_c^{\text{MIPT}}$), the subsystem appears close to a thermal state, exhibiting volume-law scaling, i.e., $S(A) \propto |A|$. At $p = p_c^{\text{MIPT}}$, the critical point, the subsystem entanglement violates the area law logarithmically, i.e., $S(A) \propto \ln |A|$.

The entanglement entropy calculation was carried out for system sizes $N = 6 - 18$. Detecting the critical point, therefore, requires finite-size scaling analysis. Inspired by prior success^{18,21-23,27,38}, we use the scaling ansatz of the following form

$$S(p, N) - S(p_c^{\text{MIPT}}, N) = F((p - p_c^{\text{MIPT}})N^{1/\nu}), \quad (8)$$

where $F(x)$ is the scaling function. In SI 1, we plot the left-hand side as a function of $(p - p_c^{\text{MIPT}})N^{1/\nu}$, and see a scaling collapse as shown in Fig. S1 also presented in the SI. Importantly, these collapses occur with the exponent of $p - p_c^{\text{MIPT}}$ set to 1. The critical parameters extracted from the numerics are listed in Table 1. We provide further details on numerics in SI 1. They show the MIPT occurs at an ansatz-specific critical value of p , up to 2.5 times larger than the $p_c^{\text{MILT}} \approx 0.2$ where, in the gradient analyses of Sec. 2.1, the BP universally collapses.

We now turn to determine the information-theoretic properties of optimization, viewing it as a communication channel as discussed in Sec. 1.1. To do so, we will compute the mutual information $I(A : B)$ between Alice’s classical information and Bob’s measurement results following the discussion in the methods section, Sec. 3.2. There are many ways of defining mutual information depending on (i) how Alice encodes her information into the quantum circuit, (ii) local operations + measurements that Bob can access to recover the classical information (iii) whether the intermediate measurements are known to Bob. The degree of information encoded in the variational parameters

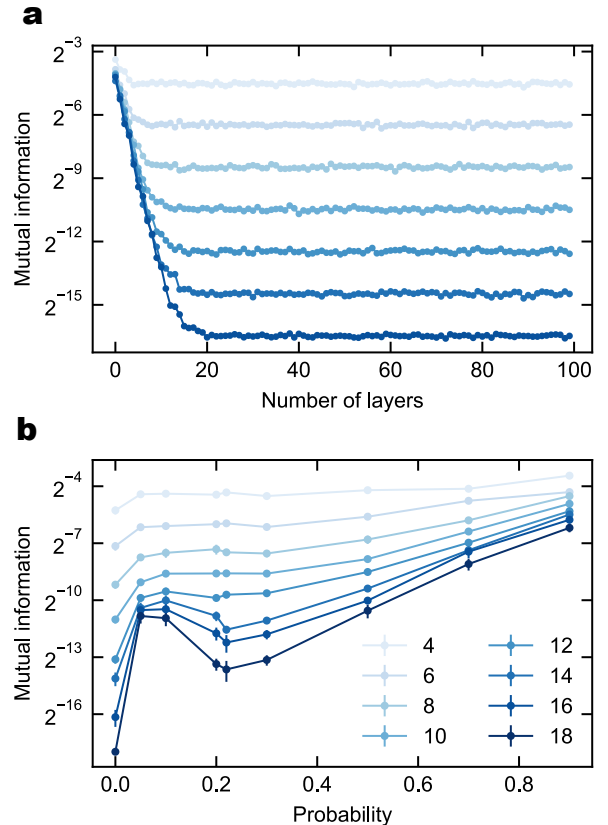


Fig. 6: Mutual information between Alice and Bob. **a** An exponential drop of mutual information $I(A : B)$ between Alice and Bob in the HEA2 ansatz with no measurements, Alice drawing parameters θ uniformly and Bob measuring $\hat{O} = \hat{Z}_0 \hat{Z}_1$. These results establish the barren plateau as a no-coding phase without measurements. **b** Mutual information for the equivalent monitored circuit at layer N , the number of qubits, post-selected for a specific set of intermediate measurement outcomes, showing three distinct regions: the mutual information immediately jumps for a finite but small p dips until around 0.2 and grows again. The second transition coincides with the MILT observed in the cost-function gradients.

that can be recovered in the cost function determines the trainability of the circuit. Thus, we consider the case in which Bob can measure the operator $\hat{Z}_0 \hat{Z}_1$ with outcomes $i = -1, 1$ with a conditional probability $p(i | \theta)$. Similarly, Alice has access to all the parameters θ of the HEA2 ansatz and chooses them with a uniform probability $p(\theta)$. Furthermore, we can insert intermediate measurement gates to the variational circuit as depicted in Fig. 2 and consider measurement outcomes M . We compute $I(A : B)$ for both circuits-with or without intermediate measurements. In particular, we consider the case where measurement outcomes are post-selected and unknown to Bob for the circuits with intermediate measurements.

We present the results for the mutual information $I(A : B)$ in Fig. 6. Fig. 6a shows $I(A : B)$, in the absence of measurements and for circuits with depth $\gtrsim N$, experiences an exponential drop in system size. Indeed $I(A : B)$ here behaves very similarly to the variance of the gradients.

Further, Fig. 6a appears nearly identical to the original results that help establish the existence of BPs⁸ up to a factor of 10 in the layer depth. Specifically, $I(A : B)$ saturates above a circuit depth of approximately 1/10 that of the saturation of the variance of the gradients. Hence, the mutual information captures the BP similarly to the variance of the gradients.

Fig. 6b presents the mutual information in the presence of measurements, post-selecting to have the specific set of outcomes $\mathbf{M} = \{0, 0, \dots, 0\}$. The specific choice of \mathbf{M} is not consequential since we average over random parameters. We find three distinct regions separated by two transitions, one right at $p = 0$ and a second at $p_c^{\text{MILT}} \approx 0.2$. The first transition is supported by the observation that at low but finite p , the mutual information quickly jumps and becomes independent of the system size. Though this low measurement rate region has a barren plateau, it is a coding phase. A code must exist, though possibly difficult to find, that enables the cost function to be sensitive to the change in parameters. The drop with system size appears again near the dip at the second transition. Though it survives beyond this transition, the overall scale grows linearly in the measurement probability. The second transition coincides with the MILT observed in the variance of the gradient as well as optimization traces. In this way, the mutual information examined here provides evidence that the trainability of a variational circuit with BP can be improved with finite but low measurement rate and post-selection. It also provides additional insights into the nature of the barren plateau (coding vs no coding) in the phase diagram shown in Fig. 7 that we discuss below.

2.4 Discussion

We close by commenting on the role of the MIPT in optimization, how measurements and the quantum Zeno effect compares to the traditional constant depth circuit approach to optimization, and finally future directions for studies of the coding BP phase.

The role of the MIPT in optimization is an important question left unanswered by our results. What behavior characterizes the intermediate region between p_c^{MILT} and p_c^{MIPT} ? Below p_c^{MIPT} there is a volume-law entanglement growth. Yet, the variance of the gradients in Fig. 3, vanishes above $p_c^{\text{MILT}} \approx 0.2$. Hence, there is no BP but there is volume law entanglement in this intermediate region. What causes the collapse of the BP? Why is the ‘‘entanglement’’ BP absent in a volume law phase?

We can partly answer the collapse of the BP question by recalling several observations. \hat{O} is a linear quantum observable and is therefore insensitive to the MIPT. Further, the mixed gradients also observe the collapse of the BP at $p = 0.2$, not just the post-selected projective gradients. So another agent than the quantum Zeno effect must be at play in this region and it causes the BP to collapse. A deeper information theoretical study of this region may reveal what this agent is.

Using a shorter circuit is an alternative to measurements to reduce expressibility and overcome the BP. Yet the two approaches are not completely unrelated.

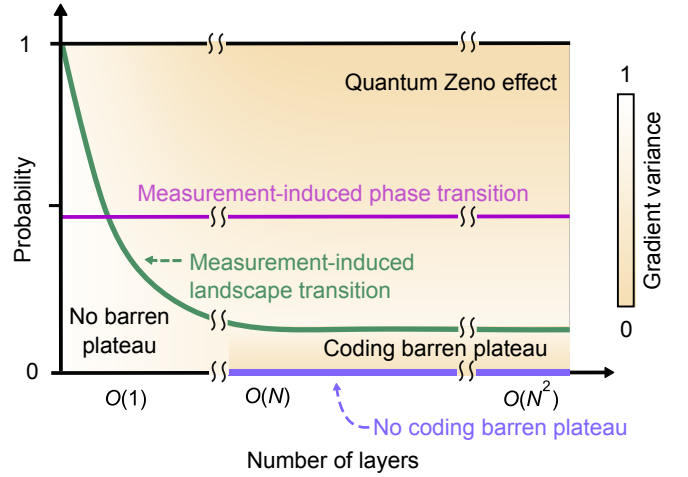


Fig. 7: Phase diagram of monitored variational quantum circuits. The variance of the gradient shows the measurement-induced landscape transition (MILT) (shown with a dark green line) between the barren plateau and the quantum Zeno regions. The variance of the gradients is maximum in the crossover region, and optimization here is the easiest. The dotted magenta line shows the measurement-induced phase transition (MIPT) for the HEA2 ansatz. Mutual information, a classical information-theoretic quantity connecting parameters to measurement outcomes, however, shows a barren plateau only near $p = 0$ (shown in solid purple line), which we call a no-coding barren plateau as Bob cannot recover the classical information encoded by Alice.

Indeed, deep in the quantum Zeno effect region, intuitively, it seems like measurements cut off the earlier circuit, leaving just a region near the end whose unitaries produce the output state. Nevertheless, by introducing intermediate measurements and post-selection, we find an improvement in the gradient’s variance as well as the mutual information. Our work thus motivates a deeper study of the circuit’s expressibility in this region, specifically comparing the two methods of controlling entanglement.

The coding barren plateau phase, among the three regions of the phase diagram, deserves the most attention in future works. The existence of the BP in both the absence and the presence of a low rate of measurements shown in the variance studies of Fig. 3, and the visualizations of Fig. 5 provide strong evidence that the BP is stable to the introduction of measurements. However, while the mutual information drops exponentially with system size at $p = 0$, it becomes finite when $0 < p < p_c^{\text{MILT}}$. It is important to note that post-selection of mid-circuit measurement outcomes was necessary for this finite mutual information, although the measurement rate can remain low, making this requirement potentially scalable. This phase, therefore, exhibits a notable contradiction: the gradients vanish, yet the cost function is still somehow sensitive to parameter changes. To leverage this change, perhaps a non-gradient-based method, like ADMM³⁹, would perform better, or an information theoretical analysis could reveal a decoder to connect parameters to the cost function.

3 Methods

3.1 Numerical Simulations

We developed a Python statevector simulation library⁴⁰ to generate our numerical results, which includes three kinds of ansatzes discussed in Sec. 1.2, namely (a) HEA1, (b) HEA2, and (c) XXZ-HVA. In each case, the simulated circuit consists of a unitary layer corresponding to a specific ansatz type followed by a layer of projective measurements with probability p per qubit. The measurements are implemented by the application of projection operators

$$P_0 = |0\rangle\langle 0| = \begin{pmatrix} 1 & 0 \\ 0 & 0 \end{pmatrix}, \quad (9)$$

$$P_1 = |1\rangle\langle 1| = \begin{pmatrix} 0 & 0 \\ 0 & 1 \end{pmatrix}. \quad (10)$$

For each measured qubit, we calculate the probability $p_0 = |\langle 0|\psi(\boldsymbol{\theta})\rangle|^2 = \langle \psi(\boldsymbol{\theta})|P_0|\psi(\boldsymbol{\theta})\rangle$ and project onto $|0\rangle$ with probability p_0 or $|1\rangle$ with probability $1 - p_0$. The results for variances and entanglement entropies presented in this paper are obtained by averaging over circuit realizations and measurement outcomes as follows:

$$\mathbb{E} \left[\langle \hat{O} \rangle_{\mathbf{M}} \right] \approx \frac{1}{N_s} \sum_{\mathcal{C}} \langle \hat{O} \rangle_{\mathbf{M}|\mathcal{C}}, \quad (11)$$

where N_s measurement outcome bitstrings (\mathbf{M}) corresponding to some circuit realization (\mathcal{C}) are sampled. Realizing a circuit \mathcal{C} consists of randomly choosing parameters from $[-\pi, \pi]$ and the location of the measurement gates. This portion of the computation involves sampling from a classical probability distribution, whereas choosing the measurement outcomes \mathbf{M} involves sampling from a quantum wavefunction. We used $N_s = 10^3$ unless specified otherwise, and the error bars were determined using a statistical bootstrapping method available in the SciPy library^{41,42}.

The numerical gradients presented in this work were calculated using analytical expressions. For example, gradient of the post-selected cost function i.e., the projective gradient can be analytically computed as follows:

$$\partial_k C_{\mathbf{M}}(\boldsymbol{\theta}) = 2\text{Re} \left[\frac{\langle \partial_k \tilde{\psi}_{\mathbf{M}} | \hat{O} | \tilde{\psi}_{\mathbf{M}} \rangle}{p_{\mathbf{M}}} - \frac{\langle \hat{O} \rangle_{\mathbf{M}}}{p_{\mathbf{M}}^2} \langle \partial_k \tilde{\psi}_{\mathbf{M}} | \tilde{\psi}_{\mathbf{M}} \rangle \right]. \quad (12)$$

A detailed derivation of this expression is given in section 3.3. We show in SI 3 this gradient can also be computed using the parameter shift method^{18,43}:

$$\partial_k C_{\mathbf{M}}(\boldsymbol{\theta}) = \frac{1}{2} \left(\langle \hat{O}_{\mathbf{M}}(\boldsymbol{\theta}^+) \rangle \frac{p_{\mathbf{M}}(\boldsymbol{\theta}^+)}{p_{\mathbf{M}}(\boldsymbol{\theta})} - \langle \hat{O}_{\mathbf{M}}(\boldsymbol{\theta}^-) \rangle \frac{p_{\mathbf{M}}(\boldsymbol{\theta}^-)}{p_{\mathbf{M}}(\boldsymbol{\theta})} \right), \quad (13)$$

where we define the shifted parameters as $\boldsymbol{\theta}^+ = \{\theta_1, \dots, \theta_k + \frac{\pi}{2}, \dots\}$ and $\boldsymbol{\theta}^- = \{\theta_1, \dots, \theta_k - \frac{\pi}{2}, \dots\}$.

Similarly, the mixed gradient can be expressed as

$$\partial_k C(\boldsymbol{\theta}) = \sum_{\mathbf{M}} 2\text{Re} \left[\langle \partial_k \tilde{\psi}_{\mathbf{M}}(\boldsymbol{\theta}) | O | \tilde{\psi}_{\mathbf{M}}(\boldsymbol{\theta}) \rangle \right]. \quad (14)$$

The mixed gradient can also be obtained by using the parameter shift method i.e.,

$$\partial_k C(\boldsymbol{\theta}) = \frac{1}{2} (C(\boldsymbol{\theta}^+) - C(\boldsymbol{\theta}^-)). \quad (15)$$

In addition to variance analysis, we performed optimization runs to minimize the energy of two cost functions: (i) $\hat{Z}_0 \hat{Z}_1$, and (ii) the XXZ Hamiltonian given by:

$$H_{XXZ} = \sum_{i=0}^N \hat{X}_i \hat{X}_{i+1} + \hat{Y}_i \hat{Y}_{i+1} + \Delta \hat{Z}_i \hat{Z}_{i+1}, \quad (16)$$

where $(N+1)^{th}$ qubit is identified with the 0^{th} qubit to impose periodic boundary. We used the L-BFGS-B algorithm⁴⁴ to optimize the HEA2 ansatz with 8 qubits, 16 layers and various measurement probabilities p . For each case, we generated 10 optimization traces starting from randomly generated initial parameters and circuit realizations.

Furthermore, we visualized the cost landscape around the optimal point. Some of the representative landscapes are shown in Fig. 5. After the convergence of our optimizer, we generated a 2d grid by taking two random vectors around the minima and evaluated the cost function at these points. We find that the cost landscape can be used as an effective tool to diagnose the trainability of an ansatz.

3.2 Estimating the mutual information of classical-quantum channels with measurements

In our setup, Alice chooses a set of parameter values $\boldsymbol{\theta}$ from a distribution $p_A(\boldsymbol{\theta}) = p_A(\boldsymbol{\theta}_1) \times p_A(\boldsymbol{\theta}_2) \times \dots \times p_A(\boldsymbol{\theta}_{|\boldsymbol{\theta}|})$, where $\boldsymbol{\theta}_j$ are independent and identically distributed (iid) variables. She then sends these parameters as input to a variational quantum circuit, that constitutes a classical-quantum channel $\boldsymbol{\theta} \mapsto \rho_{\boldsymbol{\theta}}$. Bob then carries out POVM measurements E_i and obtains the probabilities of the measurement outcomes $p(i|\boldsymbol{\theta}) = \text{Tr}[\rho_{\boldsymbol{\theta}} E_i]$. Bob is then tasked with decoding $\boldsymbol{\theta}$ from the distribution of his measurement outcomes. This sets up a classical information channel between Alice and Bob. If, along the way, measurements happen and Bob is aware of these measurement outcomes \mathbf{M} , then Bob can use this additional information to determine $\boldsymbol{\theta}$. The information channel in the case with measurements is $p(i, \mathbf{M}|\boldsymbol{\theta})$.

As stated in section 2.3, the mutual information $I(A : B)$ can be computed in numerous ways. Here, we define $I(A : B)$ to capture the training of a variational circuit; namely, Alice sends information via $p(\boldsymbol{\theta})$, and Bob receives information via measurements in the eigenbasis of a local cost function $\hat{Z}_0 \hat{Z}_1$. If the measurements occur, then one can allow Bob to access the measurement outcomes to “decode” $\boldsymbol{\theta}$. However, we focus on cases where the intermediate measurement outcomes are unavailable to Bob. We note that optimizing over Alice’s distribution $p(\boldsymbol{\theta})$ gives Shannon’s channel capacity of this classical channel.

Below, we show how to compute an efficient sample estimator for the mutual information in these circumstances.

3.2.1 No mid-circuit measurements

The probabilities of Bob's measurement outcomes in the case with no mid-circuit measurements are given by $p(i|\theta) = \text{Tr}[\rho_\theta E_i]$. The mutual information is then given by $I(A : B) = S(A) + S(B) - S(A, B)$ where S_A is the entropy of the distribution $p_A(\theta)$, $S(A, B)$ the entropy of the distribution $p(i|\theta)p_A(\theta)$ and $S(B)$ the entropy of the distribution $p_B(i) = \int d\theta p(i|\theta)p_A(\theta)$.

To compute $S(A)$ and $S(A, B)$, we must carefully treat these continuous probability distributions' entropy. We do so by discretizing the parameter space θ into K parameter values $\{\theta_1, \theta_2, \dots, \theta_K\}$, each occupying a volume $\Delta\theta$ such that $\lim_{|\theta| \rightarrow \infty} \sum_i \Delta\theta p(\theta_i) = \int d\theta p(\theta) = 1$. If V is the volume of the continuous space and $q(\theta)$ the uniform distribution over it, then $\Delta\theta = V/K$ and $q(\theta) = 1/V$. We these definitions, the entropy for finite K is approximately

$$S(A) = \log K - \int d\theta p_A(\theta) \log \frac{p_A(\theta)}{q(\theta)} \quad (17)$$

Similarly, we also find

$$S(A, B) = \log K - \sum_i \int d\theta p(i|\theta)p_A(\theta) \log \frac{p(i|\theta)p_A(\theta)}{q(\theta)} \quad (18)$$

so we can safely send $K \rightarrow \infty$ in the mutual information $I(A : B)$.

Bob's entropy $S(B)$, is computed from a discrete distribution. So we can use the standard Shannon entropy. Computing $p_B(i)$ we find

$$p_B(i) = \int d\theta p(i|\theta)p_A(\theta), \quad (19)$$

$$(20)$$

Then, we can obtain $S_B = -\sum_i p_B(i) \log p_B(i)$.

Putting these results together to compute the mutual information, we find

$$I(A : B) = -\sum_i \int d\theta p(i|\theta)p_A(\theta) \log \frac{p_B(i)}{p(i|\theta)} \quad (21)$$

$$= -\sum_{a,b} \frac{1}{N_a N_b} \log \frac{p_B(i_{b|a})}{p(i_{b|a}|\theta_a)} \quad (22)$$

Where in the last line we sample $p(i|\theta)p_A(\theta)$ by sampling $p_A(\theta)$ to get θ_a , then sampling $p(i|\theta_a)$ to get $i_{b|a}$ and introduce the notation $a|b$ here to remind us that sample i_b was obtained by first obtaining θ_a then sampling $p(i|\theta_a)$. We also sent $K \rightarrow \infty$, so the result is exact.

3.2.2 Accessible mid-circuit measurements

Let us now consider the case where the channel undergoes intermediate measurements, and Bob has access to these measurement outcomes. Here, the information channel is

$p(i, \mathbf{M} | \theta) = p(i|\mathbf{M}, \theta)p(\mathbf{M} | \theta)$ where \mathbf{M} denotes measurement outcomes. Given such a channel, we can again compute the mutual information as in the above noiseless case. So we can directly obtain $I(A : B)$ by sending $i \rightarrow i, \mathbf{M}$. The result is

$$\begin{aligned} I(A : B) &= -\sum_{i, \mathbf{M}} \int d\theta p(i, \mathbf{M} | \theta) p_A(\theta) \log \frac{p_B(i, \mathbf{M})}{p(i, \mathbf{M} | \theta)} \\ &= -\sum_{a,b,c} \frac{1}{N_a N_b N_c} \log \frac{p_B(i_{c|a,b}, \mathbf{M}_{b|a})}{p(i_{c|a,b}, \mathbf{M}_{b|a} | \theta_a)} \end{aligned} \quad (23)$$

where the last line is the sample estimator for $I(A : B)$ given θ_a drawn from $p_A(\theta)$, $\mathbf{M}_{b|a}$ drawn from $p(\mathbf{M} | \theta_a)$ and $i_{c|a,b}$ drawn from $p(i | \mathbf{M}_{b|a}, \theta_a)$.

3.2.3 Fixed mid-circuit measurements

We also consider the case where the intermediate measurement outcomes are post-selected to have a specific outcome, but Bob is unaware of the measurement outcomes. This is the case closest to a training problem because Bob is recovering all the information from the cost function and not the intermediate measurement probability distribution $p(\mathbf{M})$. The mutual information is then given by Eq. 23, but the summation over b is replaced by a single set of measurement outcomes \mathbf{M} :

$$\begin{aligned} I(A : B) &= -\sum_i \int d\theta p(i, \mathbf{M} | \theta) p_A(\theta) \log \frac{p_B(i, \mathbf{M})}{p(i, \mathbf{M} | \theta)} \\ &= -\sum_{a,b} \frac{1}{N_a N_b} \log \frac{p_B(i_{c|a,b}, \mathbf{M}_{b|a})}{p(i_{c|a,b}, \mathbf{M}_{b|a} | \theta_a)}. \end{aligned} \quad (24)$$

3.2.4 Marginalized mid-circuit measurements

Here, we marginalize over the environment's measurement outcomes. The channel is then given by $p(i | \theta) = \sum_{\mathbf{M}} p(i, \mathbf{M} | \theta)$. Hence, we can directly insert this into the mutual information of the noiseless case to obtain

$$I(A : B) = -\sum_i \int d\theta p(i|\theta)p_A(\theta) \log \frac{p_B(i)}{p(i|\theta)} \quad (25)$$

$$= -\sum_{a,b} \frac{1}{N_a N_b} \log \frac{p_B(i_{b|a})}{p(i_{b|a}|\theta_a)} \quad (26)$$

but now we need to estimate $p_B(i_{b|a})$ and $p(i_{b|a} | \theta_a)$. These are

$$p(i_{b|a} | \theta_a) = \sum_{\mathbf{M}} p(i_{b|a} | \mathbf{M}, \theta_a) p(\mathbf{M} | \theta_a) \quad (27)$$

$$= \sum_c \frac{1}{N_c} p(i_{b|a} | \mathbf{M}_{c|a,b}, \theta_a) \quad (28)$$

$$p_B(i_{b|a}) = \int d\theta p(i_{b|a} | \theta) p_A(\theta) \quad (29)$$

$$= \sum_c \frac{1}{N_c} p(i_{b|a} | \theta_c). \quad (30)$$

3.3 Calculating projective and mixed gradients of monitored quantum circuits

The first layer of unitary $\hat{U}_1(\theta_1)$ is applied to a quantum circuit initialized in the computational basis. The state of the circuit after projective measurement onto state 1 is given by

$$|\psi_1\rangle = \frac{\hat{P}_1 \hat{U}_1(\theta_1) |0\rangle}{\sqrt{p_1}}, \quad p_1 = \langle 0 | \hat{U}_1^\dagger(\theta_1) \hat{P}_1 \hat{U}_1(\theta_1) |0\rangle. \quad (31)$$

After the second layer of unitary and projective measurement onto state $\mathbf{2}$,

$$|\psi_2\rangle = \frac{\hat{P}_2 \hat{U}_2(\theta_2) \hat{P}_1 \hat{U}_1(\theta_1) |0\rangle}{\sqrt{p_2}} \quad (32)$$

$$p_2 = \langle 0 | \hat{U}_1^\dagger(\theta_1) \hat{P}_1 \hat{U}_2^\dagger(\theta_2) \hat{P}_2 \hat{U}_2(\theta_2) \hat{P}_1 \hat{U}_1(\theta_1) |0\rangle, \quad (33)$$

where $\mathbf{2} = (1, 2)$. Notice that p_1 in the denominator has cancelled out. By continuing this process for M layers, we get

$$|\psi_{\mathbf{M}}\rangle = \frac{\hat{P}_M \hat{U}_M(\theta_M) \cdots \hat{P}_1 \hat{U}_1(\theta_1) |0\rangle}{\sqrt{p_{\mathbf{M}}}} = \frac{|\tilde{\psi}_{\mathbf{M}}\rangle}{\sqrt{p_{\mathbf{M}}}}, \quad (34)$$

$$p_{\mathbf{M}} = \langle \tilde{\psi}_{\mathbf{M}} | \tilde{\psi}_{\mathbf{M}} \rangle, \quad (35)$$

where we have taken $|\tilde{\psi}_{\mathbf{M}}\rangle = \hat{P}_M \hat{U}_M(\theta_M) \cdots \hat{P}_1 \hat{U}_1(\theta_1) |0\rangle$, the unnormalized measured state. For a specific set of measurement outcomes $\mathbf{M} = (1, 2, \dots, M)$, the expectation value of an operator \hat{O} is given by:

$$C_{\mathbf{M}}(\theta) = \langle \psi_{\mathbf{M}}(\theta) | \hat{O} | \psi_{\mathbf{M}}(\theta) \rangle = \frac{\langle \tilde{\psi}_{\mathbf{M}} | \hat{O} | \tilde{\psi}_{\mathbf{M}} \rangle}{p_{\mathbf{M}}} = \frac{\langle \hat{O} \rangle_{\mathbf{M}}}{p_{\mathbf{M}}} \quad (36)$$

The ensemble average over all possible measurement outcomes is then

$$C(\theta) = \mathbb{E}[C_{\mathbf{M}}(\theta)] = \sum_{\mathbf{M}} p_{\mathbf{M}} C_{\mathbf{M}}(\theta) \quad (37)$$

We calculate the gradients of both the post-selected and averaged expectation values, starting with the post-selected:

$$\partial_k C_{\mathbf{M}}(\theta) = \frac{\partial C_{\mathbf{M}}(\theta)}{\partial \theta_k} = \frac{1}{p_{\mathbf{M}}} \frac{\partial \langle \hat{O} \rangle_{\mathbf{M}}}{\partial \theta_k} - \frac{\langle \hat{O} \rangle_{\mathbf{M}}}{p_{\mathbf{M}}^2} \frac{\partial p_{\mathbf{M}}}{\partial \theta_k} \quad (38)$$

We note that

$$\frac{\partial \langle \hat{O} \rangle_{\mathbf{M}}}{\partial \theta_k} = \langle \partial_k \tilde{\psi}_{\mathbf{M}} | \hat{O} | \tilde{\psi}_{\mathbf{M}} \rangle + \langle \tilde{\psi}_{\mathbf{M}} | \hat{O} | \partial_k \tilde{\psi}_{\mathbf{M}} \rangle, \quad (39)$$

and

$$\frac{\partial p_{\mathbf{M}}}{\partial \theta_k} = \langle \partial_k \tilde{\psi}_{\mathbf{M}} | \tilde{\psi}_{\mathbf{M}} \rangle + \langle \tilde{\psi}_{\mathbf{M}} | \partial_k \tilde{\psi}_{\mathbf{M}} \rangle \quad (40)$$

Putting them back to Eqn. 38, we get

$$\partial_k C_{\mathbf{M}}(\theta) = \frac{1}{p_{\mathbf{M}}} \langle \partial_k \tilde{\psi}_{\mathbf{M}} | \hat{O} | \tilde{\psi}_{\mathbf{M}} \rangle - \frac{\langle \hat{O} \rangle_{\mathbf{M}}}{p_{\mathbf{M}}^2} \langle \partial_k \tilde{\psi}_{\mathbf{M}} | \tilde{\psi}_{\mathbf{M}} \rangle + \text{c.c.} \quad (41)$$

By using Eqns. 34 and 36, and taking the real part, we acquire Eqn. 12. Thus, the ensemble average of the gradients is:

$$\mathbb{E}[\partial_k C_{\mathbf{M}}(\theta)] = \sum_{\mathbf{M}} p_{\mathbf{M}} \partial_k C_{\mathbf{M}}(\theta) \quad (42)$$

$$= \sum_{\mathbf{M}} p_{\mathbf{M}} 2\text{Re}\left\{ \frac{\langle \partial_k \tilde{\psi}_{\mathbf{M}} | \hat{O} | \tilde{\psi}_{\mathbf{M}} \rangle}{p_{\mathbf{M}}} - \frac{\langle \hat{O} \rangle_{\mathbf{M}}}{p_{\mathbf{M}}^2} \langle \partial_k \tilde{\psi}_{\mathbf{M}} | \tilde{\psi}_{\mathbf{M}} \rangle \right\} \quad (43)$$

To acquire the gradient of the expectation value over all possible measurements, we start with:

$$\partial_k C(\theta) = \partial_k \sum_{\mathbf{M}} p_{\mathbf{M}} C_{\mathbf{M}}(\theta) \quad (44)$$

Using Eqn. 36, we can cancel out the factor of $p_{\mathbf{M}}$, and use Eqns. 34 and 39 to arrive at the desired identity.

$$\begin{aligned} \partial_k C(\theta) &= \sum_{\mathbf{M}} \partial_k \langle \hat{O} \rangle_{\mathbf{M}} \\ &= \sum_{\mathbf{M}} \frac{\partial \langle \hat{O} \rangle}{\partial \theta_k} \\ &= \sum_{\mathbf{M}} \left\langle \partial_k \tilde{\psi}_{\mathbf{M}} | \hat{O} | \tilde{\psi}_{\mathbf{M}} \right\rangle + \left\langle \tilde{\psi}_{\mathbf{M}} | \hat{O} | \partial_k \tilde{\psi}_{\mathbf{M}} \right\rangle \\ &= \sum_{\mathbf{M}} 2\text{Re}\left\{ \left\langle \partial_k \tilde{\psi}_{\mathbf{M}} | \hat{O} | \tilde{\psi}_{\mathbf{M}} \right\rangle \right\} \end{aligned} \quad (45)$$

In practice, we calculate the sample ensemble average of either gradient. To calculate the ensemble average for an arbitrary operator \hat{O} over one circuit, we average over N_s measurement outcome bitstrings $\{\mathbf{M}'\}$ drawn from $p_{\mathbf{M}}$. i.e.

$$\mathbb{E}[O_{\mathbf{M}}] = \sum_{\mathbf{M}} p_{\mathbf{M}} \langle \hat{O} \rangle_{\mathbf{M}} \approx \frac{1}{N_s} \sum_{\mathbf{M}'} O_{\mathbf{M}'}. \quad (46)$$

This can be generalized over multiple circuit realizations like in Eqn. 11.

4 Data Availability

The data supporting the findings are available on Zenodo⁴⁰.

5 Code Availability

The code for this study is available on Zenodo⁴⁰. Instructions for installing dependencies and running the code can be found in the README file. For

further assistance, please contact the code maintainer at str36@cornell.edu.

6 Acknowledgments

We thank Sarang Gopalkrishnan, Yong-Baek Kim, Roeland Wiersema, and Juan Felipe Carrasquilla for useful discussions.

7 Author Contributions

M.J.L. and G.G. conceived the project. G.G. and S.R. performed numerical calculations. T.S. provided the code for loss landscape visualization. All authors contributed to writing the manuscript.

References

1. Preskill, J. Quantum Computing in the NISQ era and beyond. *Quantum* **2**, 79 (2018).
2. Peruzzo, A. *et al.* A variational eigenvalue solver on a photonic quantum processor. *Nature Communications* **5**, 4213 (2014).
3. McClean, J. R., Romero, J., Babbush, R. & Aspuru-Guzik, A. The theory of variational hybrid quantum-classical algorithms. *New Journal of Physics* **18**, 023023 (2016).
4. Cerezo, M. *et al.* Variational quantum algorithms. *Nature Reviews Physics* **3**, 625–644 (2021).
5. Sim, S., Johnson, P. D. & Aspuru-Guzik, A. Expressibility and entangling capability of parameterized quantum circuits for hybrid quantum-classical algorithms. *Advanced Quantum Technologies* **2**, 1900070 (2019).
6. Haug, T., Bharti, K. & Kim, M. Capacity and Quantum Geometry of Parametrized Quantum Circuits. *PRX Quantum* **2**, 040309 (2021).
7. Holmes, Z., Sharma, K., Cerezo, M. & Coles, P. J. Connecting Ansatz Expressibility to Gradient Magnitudes and Barren Plateaus. *PRX Quantum* **3**, 010313 (2022).
8. McClean, J. R., Boixo, S., Smelyanskiy, V. N., Babbush, R. & Neven, H. Barren plateaus in quantum neural network training landscapes. *Nature Communications* **9**, 4812 (2018).
9. Cerezo, M., Sone, A., Volkoff, T., Cincio, L. & Coles, P. J. Cost function dependent barren plateaus in shallow parametrized quantum circuits. *Nature Communications* **12**, 1791 (2021).
10. Wang, S. *et al.* Noise-induced barren plateaus in variational quantum algorithms. *Nature Communications* **12**, 6961 (2021).
11. Ortiz Marrero, C., Kieferová, M. & Wiebe, N. Entanglement-Induced Barren Plateaus. *PRX Quantum* **2**, 040316 (2021).
12. Mele, A. A., Mbeng, G. B., Santoro, G. E., Collura, M. & Torta, P. Avoiding barren plateaus via transferability of smooth solutions in a Hamiltonian variational ansatz. *Phys. Rev. A* **106**, L060401 (2022).
13. Grimsley, H. R., Barron, G. S., Barnes, E., Economou, S. E. & Mayhall, N. J. Adaptive, problem-tailored variational quantum eigensolver mitigates rough parameter landscapes and barren plateaus. *npj Quantum Information* **9**, 19 (2023).
14. Friedrich, L. & Maziero, J. Avoiding barren plateaus with classical deep neural networks. *Phys. Rev. A* **106**, 042433 (2022).
15. Grant, E., Wossnig, L., Ostaszewski, M. & Benedetti, M. An initialization strategy for addressing barren plateaus in parametrized quantum circuits. *Quantum* **3**, 214 (2019).
16. Patti, T. L., Najafi, K., Gao, X. & Yelin, S. F. Entanglement devised barren plateau mitigation. *Phys. Rev. Res.* **3**, 033090 (2021).
17. Sack, S. H., Medina, R. A., Michailidis, A. A., Kueng, R. & Serbyn, M. Avoiding Barren Plateaus Using Classical Shadows. *PRX Quantum* **3**, 020365 (2022).
18. Wiersema, R., Zhou, C., Carrasquilla, J. F. & Kim, Y. B. Measurement-induced entanglement phase transitions in variational quantum circuits. *SciPost Phys.* **14**, 147 (2023).
19. Nahum, A., Ruhman, J., Vijay, S. & Haah, J. Quantum Entanglement Growth under Random Unitary Dynamics. *Phys. Rev. X* **7**, 031016 (2017).
20. Li, Y., Chen, X. & Fisher, M. P. A. Quantum Zeno effect and the many-body entanglement transition. *Phys. Rev. B* **98**, 205136 (2018).
21. Li, Y., Chen, X. & Fisher, M. P. A. Measurement-driven entanglement transition in hybrid quantum circuits. *Phys. Rev. B* **100**, 134306 (2019).
22. Skinner, B., Ruhman, J. & Nahum, A. Measurement-Induced Phase Transitions in the Dynamics of Entanglement. *Phys. Rev. X* **9**, 031009 (2019).
23. Jian, C.-M., You, Y.-Z., Vasseur, R. & Ludwig, A. W. W. Measurement-induced criticality in random quantum circuits. *Phys. Rev. B* **101**, 104302 (2020).
24. Lavasani, A., Luo, Z.-X. & Vijay, S. Monitored quantum dynamics and the Kitaev spin liquid. *Phys. Rev. B* **108**, 115135 (2023).
25. Lavasani, A., Alavirad, Y. & Barkeshli, M. Measurement-induced topological entanglement transitions in symmetric random quantum circuits. *Nature Physics* **17**, 342–347 (2021).
26. Choi, S., Bao, Y., Qi, X.-L. & Altman, E. Quantum Error Correction in Scrambling Dynamics and Measurement-Induced Phase Transition. *Phys. Rev. Lett.* **125**, 030505 (2020).
27. Gullans, M. J. & Huse, D. A. Dynamical Purification Phase Transition Induced by Quantum Measurements. *Phys. Rev. X* **10**, 041020 (2020).
28. Holevo, A. S. Quantum Systems, Channels, Information: A Mathematical Introduction. ISBN: 9783110273403 (De Gruyter, Berlin, Boston, 2013).
29. Kandala, A. *et al.* Hardware-efficient variational quantum eigensolver for small molecules and quantum magnets. *Nature* **549**, 242–246 (2017).

30. Farhi, E., Goldstone, J. & Gutmann, S. A quantum approximate optimization algorithm. Preprint at arXiv:1411.4028 (2014).
31. Wecker, D., Hastings, M. B. & Troyer, M. Progress towards practical quantum variational algorithms. *Phys. Rev. A* **92**, 042303 (2015).
32. Kattemölle, J. & van Wezel, J. Variational quantum eigensolver for the Heisenberg antiferromagnet on the kagome lattice. *Phys. Rev. B* **106**, 214429 (2022).
33. Cong, I., Choi, S. & Lukin, M. D. Quantum convolutional neural networks. *Nature Physics* **15**, 1273–1278 (2019).
34. Pesah, A. *et al.* Absence of Barren Plateaus in Quantum Convolutional Neural Networks. *Phys. Rev. X* **11**, 041011 (2021).
35. Grimsley, H. R., Economou, S. E., Barnes, E. & Mayhall, N. J. An adaptive variational algorithm for exact molecular simulations on a quantum computer. *Nature Communications* **10**, 3007 (2019).
36. Gyawali, G. & Lawler, M. J. Adaptive variational preparation of the Fermi-Hubbard eigenstates. *Phys. Rev. A* **105**, 012413 (2022).
37. Li, H., Xu, Z., Taylor, G., Studer, C. & Goldstein, T. Visualizing the Loss Landscape of Neural Nets. in *Advances in Neural Information Processing Systems* (eds Bengio, S. *et al.*) **31** (Curran Associates, Inc., Red Hook, NY, 2018), 6389–6399.
38. Zabalo, A. *et al.* Critical properties of the measurement-induced transition in random quantum circuits. *Phys. Rev. B* **101**, 060301 (2020).
39. Taylor, G. *et al.* Training Neural Networks Without Gradients: A Scalable ADMM Approach. in *Proceedings of The 33rd International Conference on Machine Learning* (eds Balcan, M. F. & Weinberger, K. Q.) **48** (PMLR, New York, New York, USA, 20–22 Jun 2016), 2722–2731.
40. Gyawali, G., Rappaport, S. & Lawler, M. *Measurement-Induced Landscape Transitions and Barren Plateaus Python Library* (Oct. 2024).
41. Virtanen, P. *et al.* SciPy 1.0: Fundamental Algorithms for Scientific Computing in Python. *Nature Methods* **17**, 261–272 (2020).
42. Efron, B. & Tibshirani, R. J. An Introduction to the Bootstrap. *Monographs on Statistics and Applied Probability* **57** (Chapman & Hall/CRC, Boca Raton, Florida, USA, 1993).
43. Mitarai, K., Negoro, M., Kitagawa, M. & Fujii, K. Quantum circuit learning. *Physical Review A* **98** (2018).
44. Nocedal, J. & Wright, S. J. Numerical Optimization. 2e (Springer, New York, NY, USA, 2006).

Supplementary Information for

“Measurement-Induced Landscape Transitions and Coding Barren Plateaus in Hybrid Variational Quantum Circuits”

Gaurav Gyawali[†], Sonny Rappaport[†], Tiago Sereno, Michael J. Lawler

1 Finite-size scaling analysis of measurement induced criticality

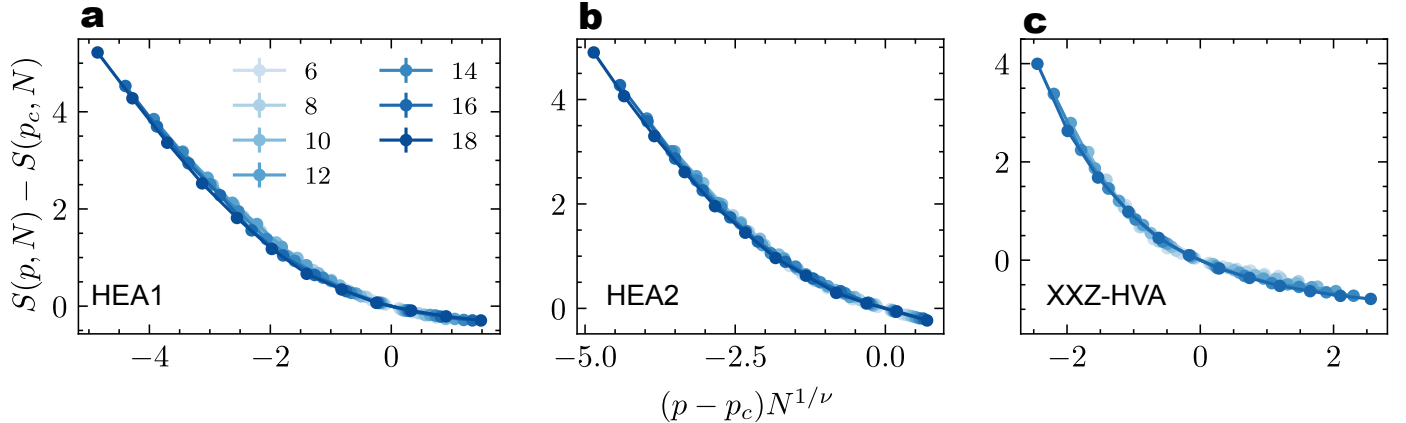


Fig. S1: Finite-size scaling data collapse of the average entanglement entropy. Entanglement dynamics starting from a computational basis state $|00 \cdots 0\rangle$ was computed for **a** HEA1, **b** HEA2, and **c** XXZ-HVA ansatz used to extract the critical probability p_c^{MIPT} , and scaling exponent ν . XXZ-HVA lacks $N = 18$ datapoints.

Although phase transitions are defined in the thermodynamic limit, we can use finite-size scaling analysis to study them numerically. With our exact state vector calculations, we were able to simulate systems only up to 18 qubits with 10^3 samples for $N \leq 16$ and 500 samples for $N = 18$. We used the quality of the data collapse to determine the critical probability p_c^{MIPT} , and critical exponent ν .

The model for the finite-size scaling collapse is given in Eqn. 8. If there is a continuous phase transition at $p = p_c^{\text{MIPT}}$, then the left hand side of this equation, computed close to p_c^{MIPT} should collapse into the scaling function of the parameter $(p - p_c^{\text{MIPT}})L^{1/\nu}$. The fitting parameters are determined by the method described in Ref. 22. We discuss this briefly for completeness.

We define a cost function $R(p_c^{\text{MIPT}}, \nu)$ for given values of critical parameters p_c^{MIPT} and ν which will be minimized to get the best estimates. $S(p_c^{\text{MIPT}}, N)$ for each system size N is determined by linear interpolation and $x = (p - p_c^{\text{MIPT}})N^{1/\nu}$, $y_N = S(p, N) - S(p_c^{\text{MIPT}}, N)$ are calculated for each data point. A family of curves $y_L(x)$ is obtained and the average of these curves calculated to get the mean $\bar{y}(x)$, to which all our data points will hopefully collapse. The cost function is defined as

$$R = \sum_{i,L} [y_L(x_i) - \bar{y}(x_i)]^2. \quad (\text{S1})$$

The fitting cost function was minimized using L-BFGS-B routine available in Scipy library to get an estimate for p_c^{MIPT} and ν . Once a good estimate was found, random initial values in their neighborhood were used as initial parameters and 5 different estimates were collected. The values reported in Table 1 are the means of those estimates and the error bars are the standard deviations. Better estimates for $N \rightarrow \infty$ can be found by iterating through the process of limiting the dataset to some N and doing a fit for p_c^{MIPT} and ν vs $1/N$ and taking the y-intercept. We did not go through this exercise since the measurement-induced entanglement phase transition is not the main topic of our study.

[†]These authors contributed equally to this work

2 Optimization traces for XXZ cost function

Here, we examine the optimization traces for a XXZ Hamiltonian with the same variational circuits. Similar to the $\hat{Z}_0\hat{Z}_1$ case of 4, we find that lower energy can be reached with a high likelihood with hybrid variational ansatzes compared to the unitary ansatzes. Before getting stuck in a quantum Zeno state, the circuits with a low probability of measurement ($p < 0.2$) explore a broader range of energy as indicated by our variance results. However, the global minimum is never reached in this case because we chose the gapless region ($\Delta < 1$) of the phase diagram for optimization. Preparing a gapless ground state with either adiabatic evolution or VQE is a considerably tricky problem compared to a gapped one.

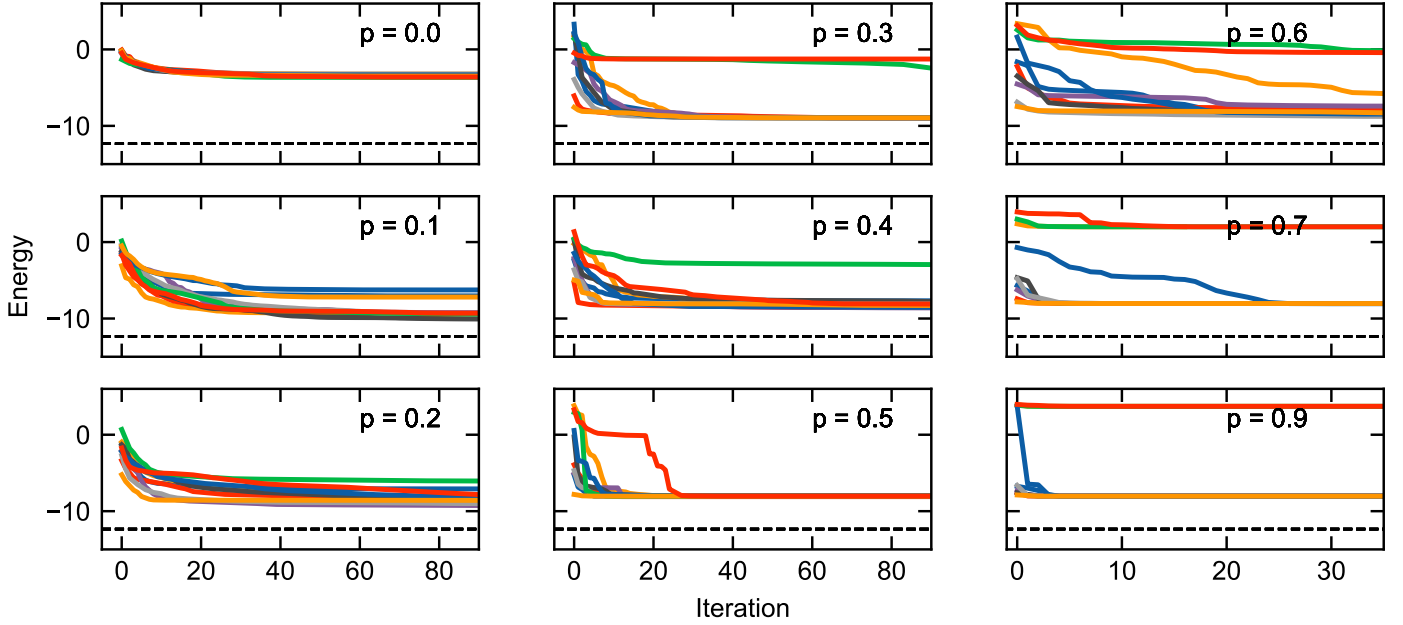


Fig. S2: Optimization with measurement and post-selection. Optimization traces are shown for an 8-qubit XXZ Hamiltonian with anisotropy parameter $\Delta = 0.5$. Each sub-figure corresponding to a measurement probability between 0 and 0.8 contains traces from 10 individual optimization runs carried out for the HEA2 ansatz with depth 20. The dashed line shows the exact ground state energy.

3 Gradients using parameter shift

Analytical gradients can be measured on a quantum computer using the parameter shift method. Let's take a closer look at Eqn. 39 :

$$\frac{\partial \langle \hat{O} \rangle_{\mathbf{M}}}{\partial \theta_k} = \langle \partial_k \tilde{\psi}_{\mathbf{M}} | \hat{O} | \tilde{\psi}_{\mathbf{M}} \rangle + \langle \tilde{\psi}_{\mathbf{M}} | \hat{O} | \partial_k \tilde{\psi}_{\mathbf{M}} \rangle. \quad (\text{S2})$$

Noting that

$$|\tilde{\psi}_{\mathbf{M}}\rangle = \left(\prod_{i=k+1}^M \hat{P}_i \hat{U}_i(\theta_i) \right) \hat{P}_l \hat{U}_l(\theta_l) \left(\prod_{i=1}^{k-1} \hat{P}_i \hat{U}_i(\theta_i) \right) |0\rangle \quad (\text{S3})$$

and

$$|\partial_k \tilde{\psi}_{\mathbf{M}}\rangle = -\frac{i}{2} \left(\prod_{i=k+1}^M \hat{P}_i \hat{U}_i(\theta_i) \right) \hat{P}_l \hat{A}_l \hat{U}_l(\theta_l) \left(\prod_{i=1}^{k-1} \hat{P}_i \hat{U}_i(\theta_i) \right) |0\rangle, \quad (\text{S4})$$

where $\hat{U}_l(\theta_l) = \exp\left(-\frac{i}{2}\theta_l \hat{A}_l\right)$. Suppose $\hat{O}' = \hat{P}_l^\dagger \left(\prod_{i=M}^{k+1} \hat{U}_i^\dagger \hat{P}_i^\dagger(\theta_i) \right) \hat{O} \left(\prod_{i=k+1}^M \hat{P}_i \hat{U}_i(\theta_i) \right) \hat{P}_l$, and $|\psi'\rangle = \hat{U}_l(\theta_l) \left(\prod_{i=1}^{k-1} \hat{P}_i \hat{U}_i(\theta_i) \right) |0\rangle$. Then,

$$\frac{\partial \langle \hat{O} \rangle_{\mathbf{M}}}{\partial \theta_k} = \frac{i}{2} \left(\langle \psi' | \hat{A}_l \hat{O}' | \psi' \rangle - \langle \psi' | \hat{O}' \hat{A}_l | \psi' \rangle \right) \quad (\text{S5})$$

$$= \frac{i}{2} \langle \psi' | [\hat{A}_l, \hat{O}'] | \psi' \rangle \quad (\text{S6})$$

The parameter-shift rule states:

$$[\hat{A}_l, \hat{O}'] = -i \left(\hat{U}_i^\dagger \left(\frac{\pi}{2} \right) \hat{O}' \hat{U}_i \left(\frac{\pi}{2} \right) - \hat{U}_i^\dagger \left(-\frac{\pi}{2} \right) \hat{O}' \hat{U}_i \left(-\frac{\pi}{2} \right) \right) \quad (\text{S7})$$

Substituting this back,

$$\frac{\partial \langle \hat{O} \rangle_{\mathbf{M}}}{\partial \theta_k} = \frac{1}{2} \left(\langle \partial_k \tilde{\psi}_{\mathbf{M}} | \hat{O} | \tilde{\psi}_{\mathbf{M}} \rangle^+ - \langle \partial_k \tilde{\psi}_{\mathbf{M}} | \hat{O} | \tilde{\psi}_{\mathbf{M}} \rangle^- \right) \quad (\text{S8})$$

$$= \frac{1}{2} \left(\frac{\langle \partial_k \tilde{\psi}_{\mathbf{M}} | \hat{O} | \tilde{\psi}_{\mathbf{M}} \rangle^+}{p_{\mathbf{M}}^+} p_{\mathbf{M}}^+ - \frac{\langle \partial_k \tilde{\psi}_{\mathbf{M}} | \hat{O} | \tilde{\psi}_{\mathbf{M}} \rangle^-}{p_{\mathbf{M}}^-} p_{\mathbf{M}}^- \right) \quad (\text{S9})$$

$$= \frac{1}{2} \left(\langle \hat{O} \rangle^+ p_{\mathbf{M}}^+ - \langle \hat{O} \rangle^- p_{\mathbf{M}}^- \right), \quad (\text{S10})$$

where $(.)^\pm$ denotes the expectation value calculated at parameter values $(\theta_1, \dots, \theta_l \pm \frac{\pi}{2}, \dots, \theta_M)$. Similarly, taking a closer look at Eq. 40:

$$\frac{\partial p_{\mathbf{M}}}{\partial \theta_k} = \langle \partial_k \tilde{\psi}_{\mathbf{M}} | \tilde{\psi}_{\mathbf{M}} \rangle + \langle \tilde{\psi}_{\mathbf{M}} | \partial_k \tilde{\psi}_{\mathbf{M}} \rangle \quad (\text{S11})$$

$$= \frac{1}{2} (p_{\mathbf{M}}^+ - p_{\mathbf{M}}^-) \quad (\text{S12})$$

Now, writing Eq. (38) in terms of parameter-shifted quantities,

$$\partial_k \langle \hat{O} \rangle_{\mathbf{M}} = \frac{\partial \langle \hat{O} \rangle_{\mathbf{M}}}{\partial \theta_k} = \frac{1}{p_{\mathbf{M}}} \frac{\partial \langle \hat{O} \rangle_{\mathbf{M}}}{\partial \theta_k} - \frac{\langle \hat{O} \rangle_{\mathbf{M}}}{p_{\mathbf{M}}^2} \frac{\partial p_{\mathbf{M}}}{\partial \theta_k} = \frac{1}{2} \left(\langle \hat{O} \rangle^+ \frac{p_{\mathbf{M}}^+}{p_{\mathbf{M}}} - \langle \hat{O} \rangle^- \frac{p_{\mathbf{M}}^-}{p_{\mathbf{M}}} \right) - \frac{1}{2} \frac{\langle \hat{O} \rangle}{p_{\mathbf{M}}} (p_{\mathbf{M}}^+ - p_{\mathbf{M}}^-) \quad (\text{S13})$$